Towards modeling of nonlinear laser-plasma interactions with hydrocodes: The thick-ray approach

A. Colaïtis,* G. Duchateau, P. Nicolaï, and V. Tikhonchuk
Université de Bordeaux 1, CNRS, CEA, Centre Lasers Intenses et Applications, UMR No. 5107, 351 Cours de la Libération, 33400 Talence, France

(Received 2 September 2013; revised manuscript received 20 November 2013; published 3 March 2014)

This paper deals with the computation of laser beam intensity in large-scale radiative hydrocodes applied to the modeling of nonlinear laser-plasma interactions (LPIs) in inertial confinement fusion (ICF). The paraxial complex geometrical optics (PCGO) is adapted for light waves in an inhomogeneous medium and modified to include the inverse bremsstrahlung absorption and the ponderomotive force. This thick-ray model is compared to the standard ray-tracing (RT) approach, both in the CHIC code. The PCGO model leads to different power deposition patterns and better diffraction modeling compared to standard RT codes. The intensity-reconstruction technique used in RT codes to model nonlinear LPI leads to artificial filamentation and fails to reproduce realistic ponderomotive self-focusing distances, intensity amplifications, and density channel depletions, whereas PCGO succeeds. Bundles of Gaussian thick rays can be used to model realistic non-Gaussian ICF beams. The PCGO approach is expected to improve the accuracy of ICF simulations and serve as a basis to implement diverse LPI effects in large-scale hydrocodes.

DOI: 10.1103/PhysRevE.89.033101 PACS number(s): 52.25.Os, 52.65.Kj, 52.35.Mw

I. INTRODUCTION

Theoretical and numerical studies of inertial confinement fusion (ICF) are supported by experiments in laser facilities worldwide. In particular, the shock ignition scheme has been studied and tests on a laser system are planned. Shock ignition requires high laser intensities, resulting in nonlinear laser-plasma interactions (LPIs) where the optical wave couples to electron and ion plasma waves, notably resulting in stimulated Raman scattering, stimulated Brillouin scattering, and cross-beam energy transfer. These nonlinear processes are commonly studied at microscopic and mesoscopic scales in particle-in-cell and paraxial electromagnetic codes, but often are omitted in larger-scale hydrodynamical codes. The importance of such effects has been highlighted by recent experiments on the National Ignition Facility and OMEGA laser facilities and supported by theoretical work and numerical simulations [1–5], constituting a strong motivation to continue including nonlinear LPI in large-scale models.

The modeling of nonlinear LPIs is based on the knowledge of the wave's electric field in the plasma. Radiative-hydrodynamic codes usually rely on ray-tracing (RT) models [6], which describe beams as bundles of needlelike rays. The RT technique is widely used in ICF codes to model the deposition of laser power in the plasma. These models are robust and easy to implement but require large amounts of CPU time. Furthermore, it is possible to model beam diffraction for vacuum or constant density conditions, using a properly adapted distribution of rays. However, because rays have no thickness, beam intensity cannot be directly computed. Consequently, this quantity is usually estimated from the inverse bremsstrahlung power absorbed by the plasma. Because rays are independent and diffraction is only modeled as an initial condition, unphysical spatial modulations arising from the mesh scale are often observed in intensity reconstructed maps. Although this behavior is not observed in simple plasma profiles, it can become very prominent in some cases. Although physical processes represented in large-scale hydrocodes often smooth out spatial modulations of laser energy deposition, nonlinear LPI processes are especially sensitive to the laser beam intensity. Therefore, it is of particular importance to describe this quantity with accuracy and robustness.

Ray-tracing models have the advantage of reducing the wave equation to a simple set of ordinary differential equations. Conversely, solving the full wave equation for the laser light in a plasma is out of the question in large-scale codes because of the numerical costs involved. There is, however, an in between, as modeling the full beam thickness and diffraction processes can be achieved by reducing the Gaussian beam diffraction problem to a set of ordinary differential equations. This type of wave problem has a large scope, including fields such as optics, geophysics, acoustics, radio physics, and plasma physics. Except for the particular case of Hamiltonian complex ray tracing [7], most available techniques reduce the above problem to complex-valued nonlinear Riccati equations. Among these methods, we note Babich and Lazutkin's solution of the abridged paraxial wave equation [8], the paraxial WKB approximation [9], complex-valued dynamic ray tracing [10,11], eikonal-based paraxial complex geometrical optics [12], and ray-based paraxial complex geometrical optics [7] (see [13] for a review).

The ray-based paraxial complex geometrical optics (PCGO) model relies on a central needlelike ray whose trajectory is determined by standard geometrical optics (GO) laws, i.e., by a RT code. The wave's electric field amplitude is then reconstructed on the central ray by integration of nonlinear Riccati-type equations. This approach is equivalent to considering a ray with a finite thickness instead of a needlelike ray. Because the PCGO method relies partially on a RT scheme, it is convenient for implementation in hydrocodes already using RT models. It is also likely to be more CPU efficient than the complex ray-tracing model because of the numerical methods that need to be implemented in that case

*Corresponding author: arnaud.colaitis@celia.u-bordeaux1.fr

[14]. The standard PCGO model is usually written in a framework where the relative permittivity is real, i.e., there are no absorption or gain processes.

We present in Sec. II the principles of PCGO and its adaptations to include absorption or gain from the medium in a self-consistent way. Validation of our implementation of PCGO in the CHIC radiative hydrocode [15] against several academic text cases is presented in Sec. III. We present in Sec. IV and Appendix A an efficient projection algorithm that allows coupling of PCGO to a hydrodynamical mesh. Applications of this projection to the inverse bremsstrahlung absorption and the modeling of the ponderomotive force as an example of nonlinear LPIs are presented in Sec. V, along with comparisons to standard RT-based results. As individual PCGO rays are limited to Gaussian modes, we present in Sec. VI an application of the use of thick rays for modeling realistic ICF beams, taking advantage of the speckles induced by laser smoothing techniques. A summary and outlook are presented in Sec. VII.

II. RAY-BASED PARAXIAL COMPLEX GEOMETRICAL OPTICS

A. Basic equations of geometrical optics

Both the RT and PCGO methods rely on GO principles. The starting point of GO is the Helmholtz equation. For a monochromatic wave, the equation for the scalar wave field $u(t,\boldsymbol{r})$ takes the form [14]

$$\Delta u(\omega,\boldsymbol{r}) + k_0^2 \epsilon(\omega,\boldsymbol{r}) u(\omega,\boldsymbol{r}) = 0, \tag{1}$$

where $u(\omega,\boldsymbol{r})$ is the electric field amplitude at frequency ω, $\boldsymbol{r}$ is the spatial coordinate, $k_0 = \omega_0/c$ is the vacuum wave vector (ω_0 being the vacuum frequency), and ϵ is the relative permittivity of the medium. The Helmholtz equation describes wave dispersion and gain via the frequency-dependent relative permittivity, composed of a real and an imaginary part and modeled by

$$\epsilon(\omega,\boldsymbol{r}) = \epsilon'(\omega,\boldsymbol{r}) + i\epsilon''(\omega,\boldsymbol{r}) = 1 - \frac{n_e}{n_c}(1 + i\nu_{ei}/\omega_0), \tag{2}$$

where n_c is the critical density, $\epsilon'(\omega,\boldsymbol{r})$ is the real part and $\epsilon''(\omega,\boldsymbol{r})$ the imaginary part of the relative permittivity, and ν_{ei} is the electron-ion collision frequency.

For a monochromatic wave, the general solution to the Helmholtz equation takes the form of an almost-plane wave

$$u(\boldsymbol{r}) = A(\boldsymbol{r}) \exp[ik_0\psi(\boldsymbol{r})], \tag{3}$$

where $A(\boldsymbol{r})$ is a slowly varying amplitude and $\psi(\boldsymbol{r})$ is the eikonal, or optical path. It is worth mentioning that in standard GO, the eikonal is a real number. The necessary conditions for this formalism to be correct are detailed in Sec. II D. The scalar field can then be expanded in inverse powers of the vacuum wave number (Debye expansion)

$$u(\boldsymbol{r}) = \left[A_0(\boldsymbol{r}) + \frac{A_1(\boldsymbol{r})}{ik_0} + \frac{A_2(\boldsymbol{r})}{(ik_0)^2} + \cdots\right] \exp[ik_0\psi(\boldsymbol{r})]. \tag{4}$$

Substituting this model into the Helmholtz equation yields equations at different orders. The zeroth order is called the eikonal equation and reads

$$(\nabla\psi)^2 = \epsilon(\boldsymbol{r}). \tag{5}$$

Higher-order terms are called transport equations and read

$$\begin{aligned} 2\nabla A_0 \cdot \nabla\psi + A_0\Delta\psi &= 0, \\ 2\nabla A_1 \cdot \nabla\psi + A_1\Delta\psi &= -\Delta A_0, \\ &\vdots \\ 2\nabla A_m \cdot \nabla\psi + A_m\Delta\psi &= -\Delta A_{m-1}. \end{aligned} \tag{6}$$

The eikonal equation belongs to the Hamilton-Jacobi variety. Using the characteristic technique yields the Hamiltonian $\mathcal{H}$ of the system

$$\mathcal{H} = \tfrac{1}{2}[\boldsymbol{p}^2 - \epsilon(\boldsymbol{r})] = 0, \tag{7}$$

where $\boldsymbol{p} = \nabla\psi$ is identified as the momentum of the ray

$$\frac{d\boldsymbol{r}}{d\tau} = \boldsymbol{p}, \quad \frac{d\boldsymbol{p}}{d\tau} = \frac{1}{2}\nabla\epsilon(\boldsymbol{r}), \tag{8}$$

where τ is linked to the elementary arclength ds by the relation $d\tau = ds/\sqrt{\epsilon'}$. These equations describe the standard trajectory of a ray and constitute the basis of the RT method. It is usually assumed that the imaginary part of the refractive index does not contribute to the trajectory of the ray. Accounting for the imaginary part of the relative permittivity can be done when $n'' \ll n'$ using a perturbation technique for the eikonal and rays. A set of equations for the perturbed ray trajectory can then be solved [14]. For the sake of simplicity, we will neglect this effect, as is done in most RT models applied to ICF.

In RT models, a large number of rays arranged to mimic spatial power profiles of realistic beams propagate in the plasma following Eqs. (8). Conversely, a Gaussian beam modeled with PCGO relies on a single ray with a nonzero thickness, resulting in the former rays sometimes being called fat rays or thick rays.

B. Principles of paraxial complex geometrical optics

The principle of PCGO is to use a central ray that follows GO trajectories as a coordinate system for the higher-order transport equations (6), which are neglected in GO. We now consider that the eikonal of the wave presented in Eq. (3) is a complex number, so the electric field possesses a decaying component in addition to the oscillatory one. In standard PCGO, we consider only the real part of the relative permittivity ϵ'.

From a central ray trajectory, computed using traditional GO, we define a new coordinate system $\{q_1,q_2,\tau\}$, where the vector $\boldsymbol{q}$ is orthogonal to the ray and τ is tangent to it. In a three-dimensional (3D) framework, this new coordinate system must account for torsion and curvature of the ray in order to constitute a rotationless orthogonal basis, providing parallel transport along the ray. Such a basis was proposed in [16] and is often referred to as Popov's ray-centered coordinate system.

The eikonal equation (3) written in the central ray coordinate system reads

$$\begin{aligned} &\frac{1}{h^2}\left(\frac{\partial\psi}{\partial\tau}\right)^2 + \left(\frac{\partial\psi}{\partial q_1}\right)^2 + \left(\frac{\partial\psi}{\partial q_2}\right)^2 \\ &\quad = \epsilon'(\boldsymbol{r}_c) + (\boldsymbol{q}\cdot\nabla)\epsilon'(\boldsymbol{r}_c) + \frac{1}{2}(\boldsymbol{q}\cdot\nabla)^2\epsilon'(\boldsymbol{r}_c) + \cdots, \end{aligned} \tag{9}$$

where $h = \sqrt{\epsilon_c'(\tau)} - (\boldsymbol{q}\cdot\boldsymbol{\nabla})\sqrt{\epsilon_c'(\tau)}$ is the Lamé coefficient (always real), $\boldsymbol{r}_c$ refers to the central ray position, and the real part of the relative permittivity $\epsilon'(\boldsymbol{r}) = \epsilon'(\boldsymbol{r}_c + \boldsymbol{q})$ has been expanded in a Taylor series in small deviations of $\boldsymbol{q} = \boldsymbol{r} - \boldsymbol{r}_c$. The transport equation (6) in the new coordinate system reads

$$\frac{2}{h^2}\frac{\partial\psi}{\partial\tau}\frac{\partial A_0}{\partial\tau} + \left[\frac{1}{h}\frac{\partial}{\partial\tau}\left(\frac{1}{h}\frac{\partial\psi}{\partial\tau} + \frac{\partial^2\psi}{\partial q_1^2} + \frac{\partial^2\psi}{\partial q_2^2}\right)\right]A_0 = 0, \tag{10}$$

where only the first term in the Debye expansion of the field is kept [Eq. (4)].

The standard model for the phase of the beam in PCGO reads

$$\psi(q_1,q_2,\tau) = \psi_c(\tau) + \tilde{\psi}(q_1,q_2,\tau), \tag{11}$$

where $\psi_c(\tau)$ is the phase of the central ray and $\tilde{\psi}(q_1,q_2,\tau)$ is the phase of the wave around the central ray, assumed to vary quadratically with q:

$$\tilde{\psi}(q_1,q_2,\tau) = \tfrac{1}{2}B_{ij}(\tau)q_iq_j, \tag{12}$$

where B is the so-called curvature matrix. Here B describes the phase variations around the center of the beam and relates to the curvature of the wave front ρ and the beam cross section w:

$$w(\tau) = \sqrt{\frac{2}{k_0\mathrm{Im}[B(\tau)]}}, \quad \rho(\tau) = \frac{\sqrt{\epsilon_c'}}{\mathrm{Re}[B(\tau)]}. \tag{13}$$

C. Paraxial complex geometrical optics and absorbing media

In order to model absorption consistently, we introduce another term in Eq. (11) and consider a complex relative permittivity

$$\psi(q_1,q_2,\tau) = \psi_c(\tau) + \psi_1(q_1,q_2,\tau) + \tilde{\psi}(q_1,q_2,\tau), \tag{14}$$

where $\psi_1(q_1,q_2,\tau)$ is a complex phase perturbation, small compared to ψ_c. The dependence on τ reflects the variation associated with the central ray and the dependence on $\boldsymbol{q}$ represents the effect of the perturbation on the beam thickness. We assume that the latter contribution can be neglected in our conditions, i.e., that the absorption of the medium does not contribute significantly to changes in beam thickness, only to beam intensity. Consequently, we have $\psi_1(q_1,q_2,\tau) \simeq \psi_{1c}(\tau)$ and $\psi_{1c}(\tau) \ll \psi_c(\tau)$.

For the sake of simplicity, we will now assume that the geometry is two dimensional, so there is only one component in $\boldsymbol{q}$ and there is no torsion on the central ray. The following analysis can be readily extended in three dimensions, as it is explained in Ref. [14] with more details on 3D PCGO in general. Introducing Eq. (14) in the eikonal equation (9) yields

$$\frac{1}{h^2}\left[\left(\frac{\partial\psi_c}{\partial\tau}\right)^2 + 2\frac{\partial\psi_c}{\partial\tau}\frac{\partial\tilde{\psi}}{\partial\tau} + 2\frac{\partial\psi_c}{\partial\tau}\frac{\partial\psi_{1c}}{\partial\tau}\right] + (Bq)^2 = \epsilon_c' + i\epsilon_c'' + q\frac{\partial\epsilon_c'}{\partial q} + \frac{q^2}{2}\frac{\partial^2\epsilon_c'}{\partial q^2}, \tag{15}$$

where we have neglected second-order terms in ψ and higher than second-order terms in q and only ϵ_c' is Taylor expanded. In this equation, it is worth detailing the terms in h^2:

$$h^2 = |\boldsymbol{h}\cdot\boldsymbol{h}| = \epsilon_c' - (\boldsymbol{q}\cdot\boldsymbol{\nabla})\epsilon_c' + \tfrac{1}{4}[(\boldsymbol{q}\cdot\boldsymbol{\nabla})\epsilon_c']^2. \tag{16}$$

Equation (15) is a mixture of different orders in ψ and q. To zeroth order in q we get

$$\frac{1}{h^2}\left[\left(\frac{\partial\psi_c}{\partial\tau}\right)^2 + 2\frac{\partial\psi_c}{\partial\tau}\frac{\partial\tilde{\psi}}{\partial\tau} + 2\frac{\partial\psi_c}{\partial\tau}\frac{\partial\psi_{1c}}{\partial\tau}\right] = \epsilon_c' + i\epsilon_c'', \tag{17}$$

where $h^2 \simeq \epsilon_c'$ and we have expanded ϵ_c in real and imaginary parts. Equating terms at zeroth order in ψ in this equation yields

$$\frac{\partial\psi_c}{\partial\tau} = \epsilon_c'. \tag{18}$$

This is the standard equation for the central ray phase in PCGO. To first order in ψ and using (18) we get

$$\frac{\partial\psi_{1c}}{\partial\tau} \simeq i\frac{\mathrm{Im}(\epsilon_c\epsilon_c')}{2\epsilon_c'} = i\frac{\epsilon_c''}{2}, \tag{19}$$

which relates the complex phase perturbation to the imaginary part of the relative permittivity, i.e., to the absorption or gain of the medium. To second order in q and using Eqs. (18) and (19) we get the Riccati equation

$$B^2 + \frac{\partial B}{\partial\tau} = -\frac{3}{4\epsilon_c'}\left(\frac{\partial\epsilon_c'}{\partial q}\right)^2 + \frac{1}{2}\frac{\partial^2\epsilon_c'}{\partial q^2} = \alpha(\tau), \tag{20}$$

where we have used $h^2 = \epsilon_c' - q\frac{\partial\epsilon_c'}{\partial q} + \frac{q^2}{4\epsilon_c'}(\frac{\partial\epsilon_c'}{\partial q})^2$ and $n'' \ll n'$.

This equation is identical to the one found in traditional PCGO and accounts for the beam diffraction and refraction. The introduction of the complex (and purely imaginary) perturbation phase ψ_{1c} on the central ray has no effect on the Riccati equation for B. Consequently, the expression for thickness and curvature radius of the wave follows the same form as in traditional PCGO [Eq. (13)].

The energy conservation equation for the amplitude A, which follows from the transport equation, is unchanged:

$$|\tilde{A}_0(\tau)| = |\tilde{A}_0(0)|\sqrt{\frac{w_0}{w(\tau)}}, \tag{21}$$

where $\tilde{A}_0(\tau) = [\epsilon_c'(\tau)]^{1/4}A_0(\tau)$ and $w_0 = w(0)$ is the initial Gaussian beam thickness. The full form of the electric field given by the model is then

$$u(q,\tau) = \frac{|\tilde{A}_0(0)|}{[\epsilon_c'(\tau)]^{1/4}}\sqrt{\frac{w_0}{w(\tau)}} \times \exp\left[ik_0\left(\frac{\mathrm{Re}(B)}{2}q^2 - \int_0^\tau \epsilon_c'(\tau)d\tau\right)\right] \times \exp\left[-k_0\left(\frac{\mathrm{Im}(B)}{2}q^2 + \int_0^\tau \frac{\epsilon_c''(\tau)}{2}d\tau\right)\right]. \tag{22}$$

This equation highlights the decaying factor in the electric field modeled with the contribution of ϵ_c''. The on-axis ray intensity then reads

$$I_0(\tau) = \frac{c\sqrt{\epsilon_c'}\epsilon_0}{2}|u(0,\tau)|^2 = \frac{c\epsilon_0}{2}|\tilde{A}_0(0)|^2\frac{w_0}{w}\exp\left(-k_0\int_0^\tau \epsilon_c''d\tau\right), \tag{23}$$

where ϵ_0 is the vacuum permittivity. Along with the intensity, width, and radius of curvature transported along a PCGO ray, the local beam frequency can be readily computed from the Doppler shift induced by plasma velocities described in the hydrodynamical part of the codes in which PCGO is implemented.

D. Validity domain

The PCGO model is based on several assumptions that must be carefully respected. There are three conditions, derived in detail in Ref. [14]. The first one, common to all GO methods (and complex GO), states that the wavelength should be small compared to the characteristic scale L_{ch} of the inhomogeneities of the plasma

$$\frac{\lambda}{L_{\text{ch}}} \ll 1. \tag{24}$$

For ICF, the wavelength of a typical 3ω beam is 0.35 μm and the characteristic scale of inhomogeneities is $\sim$10 μm, so this assumption generally holds in large-scale hydrocodes. The second condition relates to the small-angle wave approximation

$$\frac{\lambda}{w} \ll 1. \tag{25}$$

Typical ICF beams have a 350-μm radius at a focal spot with imposed small-scale modulations $\sim$2–3 μm, which are well over λ. Although it appears to be an easily respected condition, we will see that it limits other parameters. The third condition is the most restrictive one and is related to the preservation of the Gaussian profile along the propagation:

$$\frac{w}{L_{\text{ch}}} \ll 1. \tag{26}$$

This assumption is incorrect for a 350-μm beam in a typical ICF plasma but not for the speckles. Although this limitation forbids the modeling of a whole ICF beam by a single thick ray, the use of phase plates splits the beam into beamlets with different phases, thus providing an opportunity for realistic beam splitting in the PCGO model. We present in Sec. VI the principles behind this technique along with an example of a speckled beam modeled with PCGO. The full beam splitting algorithm is not within the scope of this paper.

The last assumption used in this model is $\epsilon'' \ll \epsilon'$, which may not be valid near the critical density. It should be noted, however, that this assumption is very common in all radiative-hydrodynamic codes for ICF.

III. VALIDATION: SIMPLE CASES

The PCGO technique presented in this paper has been implemented in two dimensions in the CHIC radiative-hydrodynamic code [15]. The central ray trajectory equations are computed by the RT model of CHIC [6], solving Eqs. (8). The Riccati equation for B is solved in variations, i.e., by defining P and Q such that $B = P/Q$ and solving two separate equations. Resulting equations in P and Q are integrated using an adaptive time-step Runge-Kutta scheme. First-order and second-order derivatives of the density field are computed from the hydrodynamical grid using standard least-squares fits and interpolation techniques. In terms of computer performances, the integration of the Riccati equation is very efficient, especially because only one ray is required.

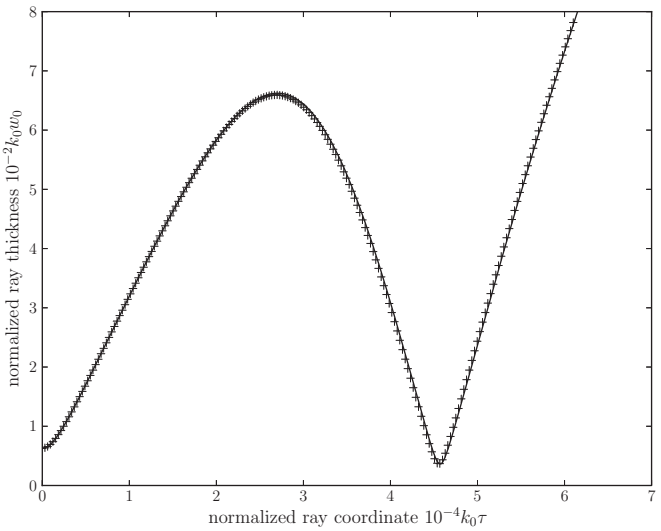

FIG. 1. Normalized radius of a thick ray incident at $\theta_0 = 30^\circ$ on a linear density ramp (θ_0 is defined with respect to the gradient axis z). Ray radius and τ coordinate are defined as in Ref. [14]. Initial conditions follow the same reference, with $w_0 = 10\lambda$, $\epsilon = 1 - bz$ (with $b = 1/1000\pi\lambda$), and $z_0 = 0$. The wavelength used here is $\lambda = 0.05/1000\pi$ m, so $\epsilon = 0$ for $z = 5$ cm. Results from PCGO in CHIC are shown as a solid line and numerical integration of the Riccati equation using the analytical form for α is shown as pluses. The latter integration is performed with MATHEMATICA with convergence monitoring and a high-accuracy goal.

Straightforward validations of the PCGO model in CHIC against theoretical diffraction solutions for Gaussian beams in vacuum and constant density media have been conducted (not shown here for conciseness). A more advanced case of a thick ray incident at 30° with respect to the normal of a linear density ramp is presented in Fig. 1. On the ascending trajectory diffraction competes against refraction, broadening the beam until refraction prevails before the turning point and on the descending trajectory where the beam starts focusing. After the focusing, with a beam waist smaller than the initial beam width, the beam width starts increasing again. The result is compared to a numerical integration of B from the analytical solution for α (see [14]) and is found to be in perfect agreement, thus validating the computation of α performed in the model.

For a beam with a plane initial wave front propagating along the axis of a waveguide medium of the form $\epsilon' = \epsilon'_0 - x^2/L^2$, one can solve analytically the Riccati equation (20) for B:

$$B_{\text{th}}^{WG} = \frac{1}{L_\perp} \frac{i\frac{L_\perp}{a_R} - \tan\frac{\tau}{L_\perp}}{i\frac{L_\perp}{a_R}\tan\frac{\tau}{L_\perp} + 1}, \tag{27}$$

where $L_\perp$ is a characteristic length and a_R is the Rayleigh length. Figure 2 shows the thickness of such a ray, as computed by our model in CHIC. Simulations are conducted for three values of the characteristic length $L_\perp$, for which the beam width oscillates when $L_\perp \neq a_R$ or is constant when $L_\perp = a_R$ (i.e., diffraction is exactly compensated by the waveguide). Paraxial complex geometrical optics results from CHIC are

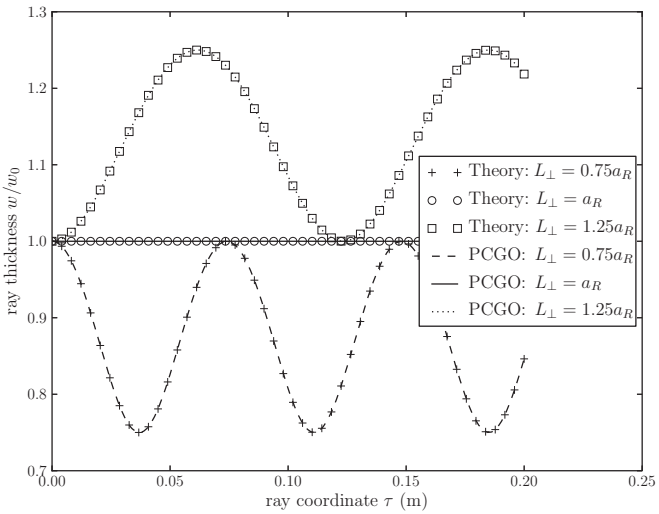

FIG. 2. Normalized radius of a thick ray propagating along the axis of a waveguide for different values of the characteristic length $L_\perp$ of the density gradient. Theoretical solutions are shown as symbols and results from the PCGO model in CHIC as lines (see the legend). The beam wavelength for this case is $\lambda_0 = 100\ \mu$m with initial radius $w_0 = 10\lambda$, so the Rayleigh length is $a_R = \pi/100$.

found to be in perfect agreement with the theoretical solution of the Riccati equation.

IV. FIELD PROJECTION

The use of PCGO rays coupled to hydrocodes opens many possibilities for large-scale simulations of nonlinear LPI. It poses, however, several technical challenges such as the efficient projection of the Gaussian beam parameters onto an irregular mesh, the configuration of which is only determined by hydrodynamical processes. It is convenient to describe the projection technique with the problem of inverse bremsstrahlung absorption.

Let us consider the case of a planar 2D geometry. The power $P^q_{\rm abs}$ deposited in the plasma by inverse bremsstrahlung in a quadrangle q of area A_q can be written

$$P^q_{\rm abs} = -\iint_{A_q} \nabla\cdot\boldsymbol{I} = \iint_{A_q} \nu_{ei}\frac{\omega_p^2}{\omega_0^2}\frac{\epsilon_0}{2}|u|^2 dA, \qquad (28)$$

where ω_p is the plasma frequency and ν_{ei} is the electron-ion collision frequency. It is convenient to split each quadrangle q into two triangles j and l to simplify density interpolations inside cells. We now refer to triangle j as the triangle in which the central ray is for $\tau \in [\tau_0,\tau_1]$, the coordinates at which it enters and leaves triangle j. We refer to triangle k as the triangle in which we perform the projection (e.g., energy deposition). These triangles can potentially be the whole hydrodynamical grid, depending on the beam configuration.

For efficient computations, we limit the beam parameter projection to triangles whose barycenters fall in the $\pm 2w$ beam envelop. The interval $[\tau_0,\tau_1]$ and the corresponding $\pm 2w$ beam envelope define a 2D surface $\mathcal{A}_j$ that intersects the Lagrangian mesh. We consider triangle k to be covered by $\mathcal{A}_j$ if there is a $\tau = \tau_{jk} \in [\tau_0,\tau_1]$ at which the normal to the central ray in triangle j passes by the barycenter of triangle k. Searches on triangles k are conducted on cells neighboring the central ray, until selected triangles are further than $\pm 2w$ away. More details on the selection criterion are included in Appendix A 1.

Once a triangle k has been selected, the power $P^k_{\rm abs}$ deposited by the beam in triangle k is simply

$$P^k_{\rm abs} = \iint_{A_k} \nu^j_{ei}\frac{\omega_p^2}{\omega_0^2}\frac{\epsilon_0}{2}|u|^2 dA, \qquad (29)$$

where A_k designates the area of triangle k and we use the value of ν_{ei} from the central ray, i.e., from triangle j, and $|u|^2 = |u_0(\tau)|^2 e^{-2r^2/w^2(\tau)}$. The natural basis in which this expression can be integrated is the ray coordinate basis $[q(\tau),\tau]$. In order to integrate this equation, we make the assumption that u, w, and $\nu_{ei}n_e/n_c$ vary linearly in $[\tau_0,\tau_1]$. Furthermore, we assume that the ray trajectory is straight in triangle j so that we can integrate in (q_s,τ), where q_s designates the normal to the straight ray. These assumptions allow us to solve analytically the first part of the surface integral along the ray-normal coordinate q. The resulting integral is computed numerically using Romberg's method. Details on the mathematical formulation and techniques used are given in Appendix A 2.

Because the projection algorithm depends on a neighbor search algorithm, its performance in terms of CPU time depends on the relative thickness of the beam compared to the mesh resolution. In the worst case scenario (which should be avoided), the beam is as large as the entire mesh, in which case the PCGO technique is of the order of RT models. Conversely, computation of energy deposition for narrow beams (with respect to the simulation domain) is much faster with PCGO than RT. The in-between performances depend on the number of RT rays used.

V. COMPARISON OF ABSORPTION AND PONDEROMOTIVE FORCE IN PCGO AND RT

A. Absorption: Density ramp

Comparisons of RT and PCGO in constant-density media (not presented here) yield similar total power deposited by the beam to the plasma. When diffraction is not introduced in RT simulations, significant differences naturally arise between initially parallel RT rays and a PCGO thick ray. The difference is larger for beams that are narrow with respect to the total simulation domain size. Ray-tracing models commonly compensate for this flaw by using a spread in the ray's initial k vectors to locally model diffraction of the beam. Rays arranged in such a configuration reproduce the global envelope of a beam as well as its intensity profile. Using this technique, similar results for the spatial profile of power deposited between PCGO and RT are obtained. It is worth mentioning that modeling diffraction of a Gaussian beam in RT codes requires a significant number of rays (we have checked that in that case, about 5000 rays are necessary), whereas the PCGO model requires only one. In general, ICF beams are very large and so is their Rayleigh length. However, nonlinear LPI effects crucially depend on diffraction modeling as a mechanism that acts against or with refraction to change the beam width and intensity. It is important to note that this method of reproducing diffraction using an initial condition

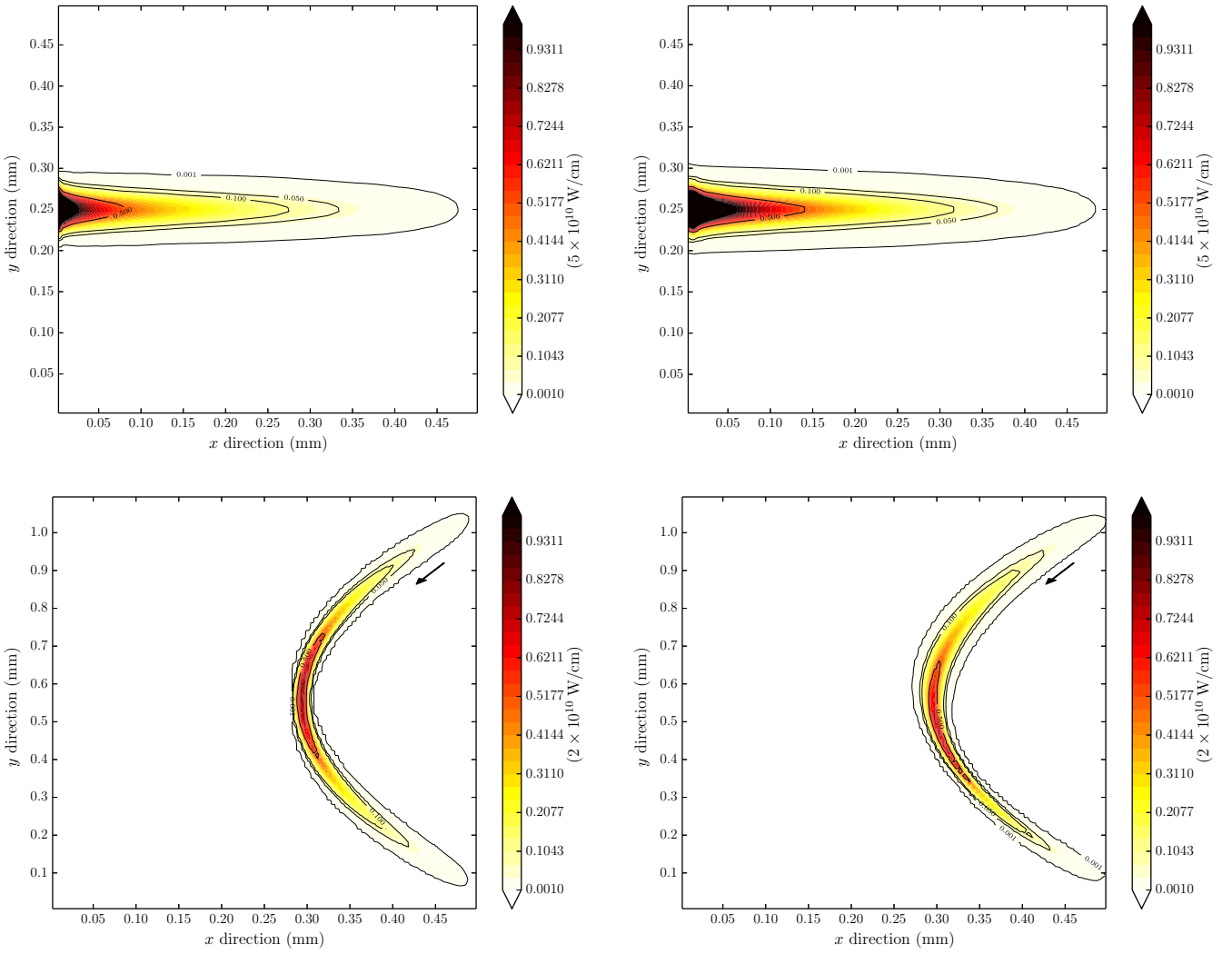

FIG. 3. (Color online) Power absorbed by inverse bremsstrahlung in a linear density ramp $n_e/n_c = 1 - 20x$ (x in cm). The initial beam width is $w = 21$ μm with zero curvature at the plasma boundary. The beam is incident from the right on the density ramp at $\theta_0 = 0^\circ$ (top) and $\theta_0 = 50^\circ$ (bottom) (see the arrow for beam direction). Figures are from a standard ray-tracing model (left) and the PCGO model (right).

on the ray's vectors is exact only for vacuum conditions (or a constant density plasma). Any departure from these conditions will not be reflected with a change in diffraction strength for the beam modeled with RT. Because rays are independent, RT-based diffraction remains that of the initial condition, i.e., that of a beam in a vacuum. This difference is highlighted in what follows with an example of inhomogeneous plasma.

We compare energy deposited in a linear density ramp of the form $n_e/n_c = 1 - X/L$, where $L = 0.5$ mm. The simulation domain is 100×100 grid points in a box of 0.5×0.5 mm^2 for an incident beam at an angle $\theta_0 = 0^\circ$ and 0.5×1.0 mm^2 for $\theta_0 = 50^\circ$. The beam's initial thickness is $w_0 = 21$ μm. The RT model is initialized so as to reproduce the caustic of the beam, with a focal length $f = 40$ m and diameter of the lens of $D = 1.27$ m. Ten thousand rays are used for the RT model. The beam's initial power is $P_0 = 1.209 \times 10^{13}$ W/cm. The energy deposited in the mesh by a beam normal to the density gradient at $\theta_0 = 0^\circ$ reads [17]

$$P_{\text{abs}}^{\text{th}} = P_0 \left[1 - \exp\left(\frac{-32 \nu_{ei}(n_c) L}{15c} \right) \right], \qquad (30)$$

where the value of $\nu_{ei}(n_c)$ in CHIC for these conditions is $\nu_{ei}(n_c) = 4.578 \times 10^{11}$ s^{-1} and $L = 500$ μm, which yields a theoretical absorption coefficient $\eta_{\text{abs}}^{\text{th}} = P_{\text{abs}}^{\text{th}}/P_0 = 80.4\%$.

The top line in Fig. 3 shows the simulation results for $\theta_0 = 0^\circ$. The total power deposited with both codes yields an absorption coefficient identical to and conforming with the theory, i.e., $\eta_{\text{abs}} = 80.4\%$. The discretized nature of the RT model (top left) leads to a slightly sharper energy deposition and underestimation of the spatial distribution of the beam. The PCGO ray thickness, corresponding to theoretical solutions, is shown in Fig. 4 (top). Diffraction effects broaden the beam and the spatial distribution of deposited power is larger for PCGO (top right).

The bottom line in Fig. 3 shows the simulation results for $\theta_0 = 50^\circ$. The total absorption coefficient with both codes is identical: $\eta_{\text{abs}} = 16.4\%$. Results from the PCGO model (bottom right) conform to the theory (see Sec. III), showing a peak power offset from the maximum density with $P_{\text{max}}^{\text{PCGO}} \simeq 1.52 \times 10^{10}$ W/cm [see Fig. 4 (bottom)]. This shift is the consequence of modeling refraction and diffraction of a single Gaussian beam, compared to many needlelike independent

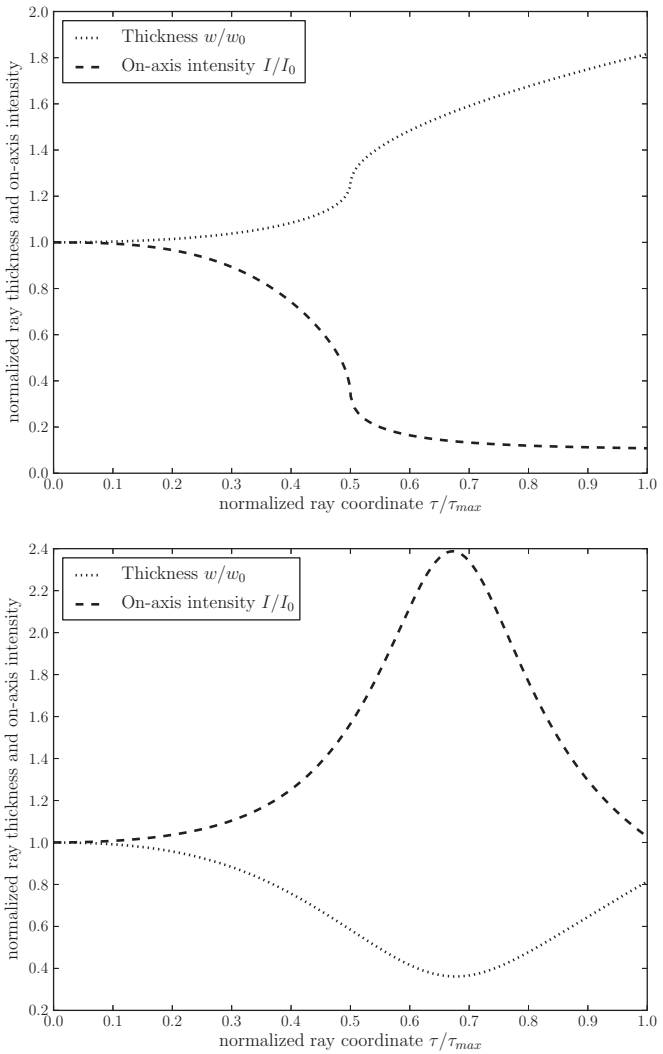

FIG. 4. The PCGO ray normalized radius (dotted lines) and normalized on-axis intensity (dashed lines), normalization with respect to initial values, for the linear density ramp with $\theta_0 = 0^\circ$ (top) and $\theta_0 = 50^\circ$ (bottom). The ray coordinate τ is normalized with respect to the maximum τ, at which the ray leaves the plasma. Here $\tau/\tau_{\max} = 0.5$ corresponds, respectively, to the reflection (top) and turning point (bottom) of the ray.

rays. In the RT model (bottom left), all rays converge to the same $\hat{x}$ coordinate, leading to a beam waist at maximum n_e/n_c (minimum $\hat{x}$). The RT model produces an artificial beam waist following from the geometrical configuration of the rays and does not reproduce the shifted waist of the beam. The peak deposited power in RT is overestimated, with $P_{\max}^{\mathrm{RT}} \simeq 1.66 \times 10^{10}$ W/cm, due to the discretized nature of the rays. Diffraction modeling in RT models is exact only for constant density media. Once variations appear in the density profile, because each ray independently follows its trajectory, diffraction may be locally underestimated or overestimated. Although the PCGO model corresponds to the exact solution in this specific case, the peak deposited power between RT and PCGO is different by only 9%. From the energy deposition standpoint only, the difference between RT and PCGO is relatively minor and likely to be smoothed by other physical processes. The underlying intensity difference and the lack of exact diffraction modeling more strongly impact nonlinear LPI modeling, as is shown in the following section.

B. Ponderomotive self-focusing

Self-focusing is a nonlinear LPI process in which spatial gradients of dielectric permittivity induced by the wave field lead to the beam refraction [18]. There are two contributions to self-focusing: thermal and ponderomotive. Both processes stem from electric field nonuniformities. In thermal self-focusing, this nonuniformity leads to temperature gradients between the beam center and its wings, creating thermally induced pressure. Hydrodynamical processes lead to on-axis density depletion, which causes beam self-focusing through a lenslike index of refraction. In ponderomotive self-focusing, the on-axis density depletion is caused by the ponderomotive force expelling the electrons.

We study the case of ponderomotive self-focusing, modeled using the RT and PCGO approaches. In order to estimate the laser intensity in RT models, it is common to use the power absorbed by the inverse bremsstrahlung as a proxy, along with the cells surface area. This technique allows us to approximate the laser intensity field and is used in most RT-based hydrocodes that include nonlinear LPI effects. The RT intensity reconstruction is implemented in CHIC for a comparison with the PCGO model. We describe in this section an implementation of the ponderomotive force directly based on the electric field modeled by the PCGO technique and compare it to the ponderomotive force estimated from RT intensity reconstruction.

1. Ponderomotive force

In a hydrodynamical approach, the ponderomotive force $F_P = -\nabla U$ acting on the electron fluid can be expressed as a gradient of the ponderomotive potential U,

$$U = \frac{e^2}{4m_e\omega_0^2}|u|^2. \tag{31}$$

In this form, the ponderomotive force can be modeled in a hydrocode as an additional pressure term U in the plasma equation of motion. We compute the mean value of U in quadrangle q from the triangle mesh

$$\langle U_q \rangle = \frac{S_{q_1}\langle U \rangle_{q_1} + S_{q_2}\langle U \rangle_{q_2}}{S_{q_1} + S_{q_2}}, \tag{32}$$

where $\langle U \rangle_{q_1}$ and $\langle U \rangle_{q_2}$ are mean values corresponding to each triangle in cell q. The ponderomotive potential in triangle i of cell q reads

$$\langle U \rangle_{q_i} = \frac{e^2}{4m_e\omega_0^2}\frac{1}{S_{q_i}}\iint_{S_{q_i}} |u|^2 dS, \tag{33}$$

where the integral over triangle i is computed in the same way as for Eqs. (A8) and (A10), assuming ϵ'' to be constant within a cell.

2. Estimating LPI in RT codes

In RT methods, the notion of ray intensity does not exist. A straightforward way to estimate the electric field associated

with a distribution of needlelike rays rely on the conservation equation for the laser energy

$$\frac{\partial \Omega}{\partial t} + \nabla \cdot \mathbf{I}_L = -\nu_{ei} \frac{n_e}{n_c} \Omega, \tag{34}$$

where $\mathbf{I}_L$ is the Poynting vector and Ω the electromagnetic energy density $\Omega = \epsilon_0 |u|^2/2$. At a given hydrodynamical time step, the laser propagation is stationary, so the first term can be neglected. We integrate over triangle k by assuming constant u, Ω and n_e/n_c. Using the Stokes formula, Eq. (34) then reads

$$\iint dS_k \nabla \cdot \mathbf{I}_L = \int \mathbf{dl} \cdot \mathbf{I}_L = -\Delta P^k_{\text{abs}} = -\nu_{ei} \frac{n_e}{n_c} \frac{\epsilon_0}{2} |u|^2 \Delta S_k, \tag{35}$$

with ΔP^k_{abs} the total power absorbed in triangle k and ΔS_k the area of triangle k. Rearranging, the ponderomotive potential estimated from RT absorption reads

$$\langle U \rangle_{q_i} = \frac{1}{2\nu_{ei}} \frac{\Delta P^{q_i}_{\text{abs}}}{\Delta S_{q_i}}. \tag{36}$$

This method can be adapted to other nonlinear LPIs that require the knowledge of the electric field, such as cross-beam energy transfer.

3. *Comparisons of ponderomotive self-focusing between PCGO and RT*

We consider a Gaussian beam in a 2D geometry with a focal spot size $w_0 = 20\lambda$ and $\lambda = 1.05$ μm. In such a configuration, the initial diffraction of the beam is relatively low, as it would be for an ICF beam. The hydrogen plasma with $T_e = 10T_i = 5$ keV and $n_e/n_c = 0.1$ is described by 180×180 grid points in a box of 2×0.2 mm^2 size. Based on the work of [19,20], we have derived in Appendix B 2 an expression for the critical power of a Gaussian beam undergoing ponderomotive self-focusing in an initially constant density plasma. The theory described in Appendix B is valid for $n_e/n_c \ll 1$ and the steady-state regime. The simulation is run for 200 ps, when the self-focusing has reached a steady state. Under these conditions, the critical power for a purely ponderomotive self-focusing is $P_C = 445.3$ MW. We consider five cases where $P/P_C = [1; 2; 3; 4; 5]$. Ray-tracing runs are conducted with 10 000 rays and diffraction modeling. Simulations yield very similar results using 5000 rays, suggesting a weak dependance on the number of rays above 5000.

a. Intensity profiles. Figure 5 (top) illustrates the RT maximum intensity in the transverse direction as a function of propagation direction z, at $t = 200$ ps, reconstructed from absorption. Although there is no clear intensity peak, partial self-focusing occurs for all cases. The self-focusing distance decreases when power increases for simulations ranging from $P/P_C = 1$ to 3 and remains similar at higher powers. The intensity amplification peak is also similar for all cases with $P/P_C \geqslant 2$. Theoretical values for intensity amplification and self-focusing distance, derived in Appendix B 1, are superimposed as colored pluses. Theoretical values show a clear dependence on the beam power to intensity amplification ratio and self-focusing distance, a dependence that the RT-based model does not reproduce. The RT intensity reconstruction requires a large number of rays per cell. Even when this condition is fulfilled, rays tend to get trapped in density channels, thus creating local waveguides, the thicknesses of which are determined by the mesh resolution (see Sec. IIIB3b). Although this phenomenon resembles filamentation, RT is not expected to model that process and it is a numerical artifact. Furthermore, once RT filamentation has started, rays tend to stay trapped because there is no more energy deposition outside the channels. Because of these limitations, the ponderomotive force from intensity reconstruction presents spatial modulations and large inaccuracies, leading to the observed discrepancies in self-focusing length and intensity amplification.

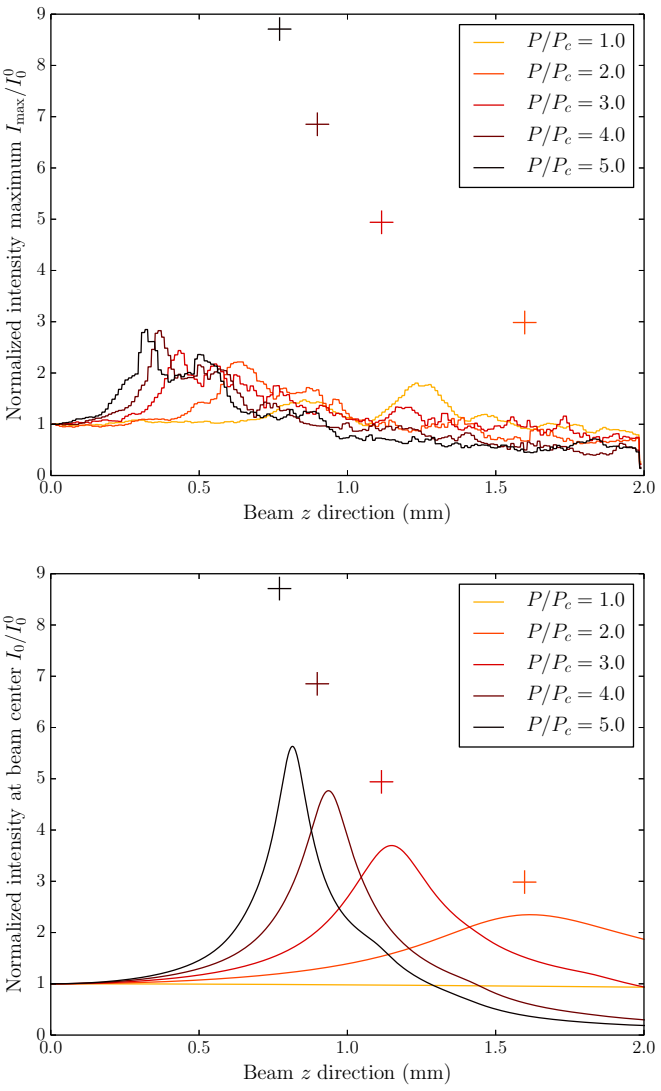

FIG. 5. (Color online) Plot of the RT-based reconstructed maximum intensity (top) and PCGO central ray intensity (bottom), as a function of the beam propagation direction z, after 200 ps of simulation for the five cases. Intensities are normalized to the initial central ray intensity $I_0(\tau = 0)$. Theoretical values for intensity amplification and self-focusing distance, derived in Appendix B 1, are superimposed as colored pluses.

Results using PCGO are illustrated in Fig. 5 (bottom), showing the normalized central ray intensity I_0/I_0^0 as a function of propagation direction z at $t = 200$ ps. We note that

for $P/P_C = 1$, the beam intensity is constant, corresponding to an equilibrium between diffraction and refraction from the waveguide created by the ponderomotive force. We find that self-focusing distances are well reproduced with thick rays and intensity amplification ratios are underestimated. Because the ponderomotive force acts along the whole beam thickness, the width of the created waveguide is of the same order. Consequently, the assumption of a small beam thickness compared to plasma inhomogeneity ($w \ll L_{\rm ch}$) is less accurate. This leads to an underestimation of the density curvature in the waveguide and of the refraction process. Although intensity amplification is underestimated, it follows the same tendency of higher amplification for higher powers as predicted by the theory. Furthermore, a departure from $w \ll L_{\rm ch}$ due to the ponderomotive force is unlikely for realistic ICF beams modeled with PCGO, as the latter contain spatial intensity modulations and are constructed from smaller thick rays (see Sec. VI). We note that in simulations with paraxial electromagnetic codes (see, for example, [21]), the beam structure after focusing is strongly distorted. Nevertheless, the focusing length and the intensity amplification are in agreement with our model.

b. Density channel. In the setup described above, simulations are run with the modulation wavelength equal to 20 Debye lengths and $Z = 1$, so acoustic wave damping can be neglected. For a nonisothermal plasma ($T_e \gg T_i$) with a weak ion damping, one transverse direction, and no thermal effects, the paraxial wave equation possesses an analytical solution for the density perturbation caused by the ponderomotive force [22]:

$$\delta n(t,x) = \frac{1}{2cn_cT_e}\left[-I(x) + \frac{1}{2}[I(x+c_st) + I(x-c_st)]\right], \tag{37}$$

where $\delta n(t,x) = n_e(t,x)/n_e(0) - 1$. Hence, we expect a central channel formation with a depletion factor of $-0.5I_0/cn_cT_e$ and two positive density perturbations (bumps) propagating away from the beam axis with a factor $0.25I(x + c_st)/cn_cT_e$. Figure 6 (top) illustrates the density perturbation along the transverse direction of a PCGO ray for $z = 0.3$ mm, normalized to cn_cT_e/I_0. The density perturbation is in good agreement with the theory for all cases. Figure 6 (bottom) shows corresponding results using the RT model. Although results are similar to the theory for $P/P_C = 1$, increasing beam power leads to the formation of local waveguides modulated by the mesh resolution. Rays are trapped in the minima for δn and self-focusing does not occur at the beam scale.

Both RT and PCGO models predict similar density depletions at a low power, but the RT model quickly grows unstable with respect to the self-focusing instability. Intensity profiles modeled using PCGO are smooth and remain Gaussian, which allows for a better code robustness. Conversely, nonlinear LPI effects modeled with RT codes are potentially subject to the same kind of instabilities and spatial modulations, which constitute the main motivation for the development of alternatives such as PCGO. This kind of spiked profile RT-based code can also be observed due to thermal effects from inverse bremsstrahlung absorption. When energy deposition is taken into account, large-scale hydrocodes usually include electronic conduction schemes that greatly smooth out these profiles, hence reducing the impact of this behavior. We stress here that in the purely ponderomotive case, this profile is a direct consequence of the spiked reconstructed intensity, which is the key quantity for LPI modeling.

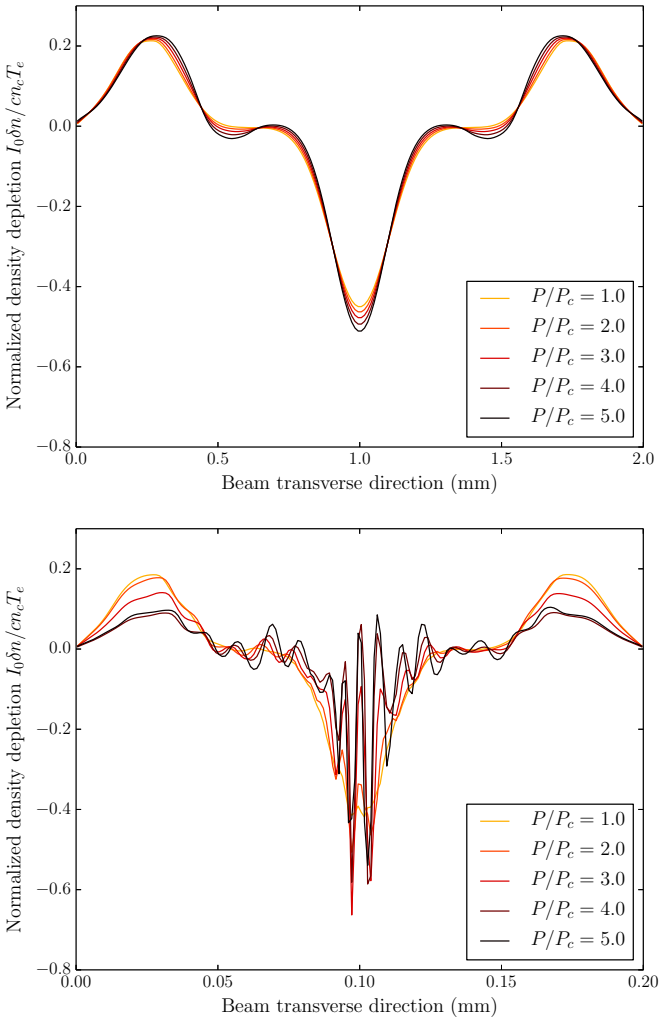

FIG. 6. (Color online) Density perturbation $\delta n(t,x) = [n_e(t,x)/n_c - 0.1]/0.1$ along the transverse to the beam, normalized to cn_cT_e/I_0, at $z = 0.3$ mm, after 100 ps. The results are from PCGO (top) and RT (bottom) models. The density anomaly in the RT case is normalized to the maximum intensity, as there is no central ray intensity. The initial beam power with respect to P_C ranges from 1 to 5.

VI. REALISTIC BEAM MODELING

The thick-ray model has been applied so far to single Gaussian beams. Modeling a typical ICF beam by a single thick ray is not realistic and does not respect the assumptions presented in Sec. II D. We briefly describe in this section the application of multiple thick rays with Gaussian profiles for ICF beam modeling. Typical ICF beams have top-hat profiles at the lens or grating and go through phase plates, resulting in various speckled intensity profiles at a focal point. Ray-tracing codes can reproduce the super-Gaussian intensity envelope observed at the focal spot and account for a global beam

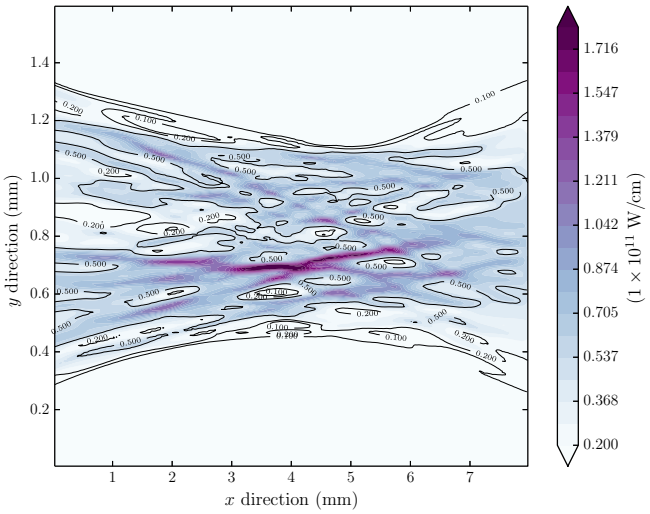

FIG. 7. (Color online) Intensity distribution obtained with the 2D PCGO model, mimicking the SG4 OMEGA beam near its focal point. Here 140 thick rays are randomly focused in a box surrounding the focal spot, the dimensions of which are characterized by the theoretical interaction of the small and large scales of the beam. The intensity is normalized to 10^{11} W/cm. An arbitrary power of 250 MW was used for the simulation.

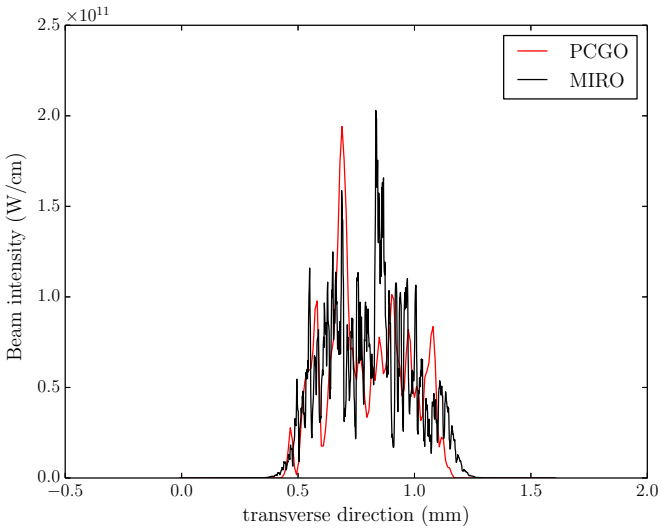

FIG. 8. (Color online) Intensity profiles comparisons between PCGO [gray (red)] and MIRO (black), at the focal spot. Results from MIRO are convoluted to the hydrodynamical mesh resolution. An arbitrary power of 250 MW was used for the simulation.

diffraction using the same technique as in Sec. V, but do not model statistical intensity fluctuations.

As an example, we consider a high-order Gaussian beam smoothed by a kinoform phase plate (KPP) and focused through a lens to the focal spot. The propagation of such a beam can be characterized by two scales [23]: the global envelope scale, where variations are determined by a modified Rayleigh length, and the scale of statistical fluctuations of the field, related to the length of speckle spots in the longitudinal direction. These two scales characterize the propagation of a partially coherent beam.

Knowing the shape of the super-Gaussian envelope at the lens, the profile of the beam envelope is computed at a distance close to the focal spot, e.g., at the hydrodynamical mesh boundary. The resulting profile is subdivided into a sum of Gaussian modes that are randomly focused following a pseudorandom multivariate normal distribution for focal spots positions. Each of these beamlets is modeled as a thick ray whose waist size is several times the speckle radius and profile is Gaussian.

Figure 7 illustrates the intensity distribution obtained with this technique in vacuum, using the OMEGA beam profile at the focal spot with the exponent order $n = 4.1$ and a radius $w = 352$ μm. We note that although the result is displayed on the hydrodynamical mesh of CHIC, this intensity map is actually obtained in vacuum. The global envelope of the beam is reproduced and corresponds to the thickness of a partially coherent beam. Intensity fluctuations are broader than the actual correlation length of the real OMEGA beam. This is inherent to the size of the hydrodynamical mesh grid and larger than the speckle width, which spatially smoothes the intensity field. Consequently, instead of reproducing the exact beam speckle pattern at the focal spot, we choose to reproduce its main features, i.e., its caustics and the overall statistics of the speckles, through the contrast. The latter parameter can be set by tuning the rays' thicknesses at the focal spot. Figure 8 illustrates an intensity slice taken along the transverse direction at the focal spot. Paraxial complex geometrical optics results are compared to the laser propagation code MIRO [24–26], resolving the nonlinear Schrödinger equation. Results from MIRO are obtained using the same KPP and are convoluted with the hydrodynamical mesh resolution. Both profiles have similar contrasts, with $C_{\mathrm{PCGO}} = 0.62$ and $C_{\mathrm{MIRO}} = 0.57$, where the contrast is defined as

$$C = \frac{\langle I^2 \rangle - \langle I \rangle^2}{\langle I \rangle^2}. \tag{38}$$

For the chosen focusing setup (focal length $f = 1.8$ m and lens diameter $\Phi = 270$ mm), the estimated speckle radius at the focal spot is 2.3 μm, so the number of modes is about 140. Results presented above are obtained using 140 thick rays with individual waist sizes of 23 μm, i.e., a ten-speckle radius and about 65λ, which is well within the limitations of the PCGO presented in Sec. II D.

VII. CONCLUSION

Nonlinear laser-plasma interactions have been implemented in a large-scale radiative hydrocode. We adapted the paraxial complex geometrical optics method to the description of laser energy deposition. Modifications needed to include absorption effects and an efficient technique for projecting the beam field onto a Lagrangian hydrodynamical mesh have been introduced.

The thick-ray model presented here and implemented in the hydrocode CHIC allows us to evaluate the beam electric field, radius of curvature, thickness, and intensity at all points in the plasma. The model consistently takes into account diffraction and absorption by inverse bremsstrahlung and is validated against several comprehensive test cases. Comparisons with

the standard RT highlights the advantages of a laser description that takes into account diffraction and refraction on index gradients. Considering energy deposition only, the RT is found to yield robust results compared to PCGO and its shortcomings are not fundamentally detrimental to large-scale hydrocodes, notably because of other processes that act to smooth energy deposition, such as electron thermal conduction.

Application to modeling nonlinear LPI was illustrated with the ponderomotive self-focusing in both the RT and PCGO frameworks. A pressure term corresponding to the ponderomotive potential was added in the hydrodynamical core. The PCGO model was validated against theoretical results for transverse density depletion and yielded the correct ponderomotive self-focusing critical power, self-focusing distance, and an intensity amplification with a correct tendency. These results were compared to the standard intensity reconstruction technique used in RT codes. It was found that the needlelike nature of RT rays leads to artificial filamentation of the beam inside local waveguides, which prevents the correct modeling of self-focusing distance and beam intensity amplification. Although RT codes can include diffraction modeling, the latter is exact only for constant density cases and does not compensate for shifts in the beam focus and curvature radius due to nonconstant refraction indexes. These shortcomings lead to incorrect estimations of laser light intensity and decrease the accuracy of nonlinear LPI modeling using RT models.

The comparisons presented in this paper were conducted using a single Gaussian beam. We presented adaptations that can be made in order to use several smaller thick rays to model one full speckled ICF beam, thus reproducing the beamlet pattern induced by the use of a phase plate. Such an adaptation yields similar spatial intensity maps at the focal point compared to the MIRO code for the OMEGA SG4 beam, thus linking a single Gaussian thick ray to realistic ICF beam modeling in hydrocodes.

The thick-ray model is expected to be an improvement in accurately modeling nonlinear LPI in large-scale hydrocodes. This model can be used to reproduce ICF beams in realistic conditions of direct drive implosion and study cross-beam energy transfer in 2D geometries.

ACKNOWLEDGMENTS

The authors wish to thank Guy Schurtz, Jérôme Breil, and Xavier Ribeyre for many useful discussions and Pierre Forestier-Colleoni for his previous work on novel approaches to the Ray-Tracing model. We warmly thank the two anonymous reviewers for their very helpful and constructive comments. This work was partially supported by the EURATOM within "Keep in Touch" activities and Project No. ANR-12-BS04-0006-04 from the French National Agency of Research.

APPENDIX A: DETAILS ON BEAM PARAMETER PROJECTION

1. Triangle selection criterion

We have defined in Sec. IV the surface $\mathcal{A}_j$ defined by the interval $[\tau_0,\tau_1]$ when the central ray is in triangle j and the corresponding $\pm 2w$ beam envelope. Figure 9 illustrates

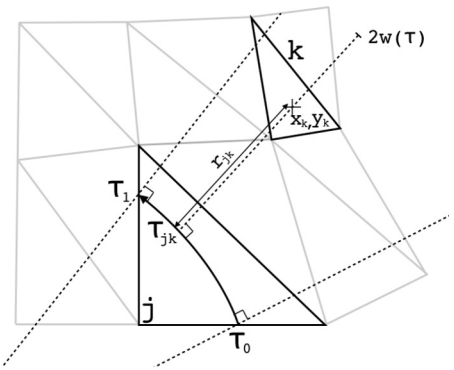

FIG. 9. Illustration of the selection process for a triangle k when the ray is in triangle j. The ray is illustrated for $\tau \in [\tau_0,\tau_1]$ as a curved arrow. Other triangles of the hydrodynamical grid are shown in gray. Dashed lines represent the ray normals at τ_0 and τ_1.

the selection criterion: A triangle k must be accounted for in the beam parameter projection of surface $\mathcal{A}_j$ if there is a $\tau = \tau_{jk} \in [\tau_0,\tau_1]$ at which the normal to the central ray in triangle j passes by the barycenter of triangle k.

The central ray trajectory in triangle j is known analytically for a constant density gradient. The eikonal equation yields the central ray position (x,y) and velocity (v_x,v_y):

$$\begin{aligned} x(\tau) &= a_x(\tau-\tau_0)^2 + v_{x0}(\tau-\tau_0) + x_0, \\ y(\tau) &= a_y(\tau-\tau_0)^2 + v_{y0}(\tau-\tau_0) + y_0, \\ v_x(\tau) &= 2a_x(\tau-\tau_0) + v_{x0}, \\ v_y(\tau) &= 2a_y(\tau-\tau_0) + v_{y0}, \end{aligned} \tag{A1}$$

where velocities are normalized to $c=1$ and a_x and a_y are hydrodynamical characteristics of the triangles, defined by

$$a_x = -\frac{1}{4n_c}\nabla_x n_e, \quad a_y = -\frac{1}{4n_c}\nabla_y n_e. \tag{A2}$$

The barycenter of triangle k, (x_k^b, y_k^b), is on the ray normal for $\tau = \tau_{jk}$ that satisfies

$$\mathbf{T}_c(\tau) \cdot \begin{pmatrix} x_k - x(\tau) \\ y_k - y(\tau) \end{pmatrix} = 0, \tag{A3}$$

where $\mathbf{T}_c(\tau)$ is the tangent vector to the central ray at τ. This equation can be expressed as a third-order polynomial in τ:

$$\begin{aligned} &-2\tau^3\left(a_x^2+a_y^2\right) - 3\tau^2(a_x v_{x0} + a_y v_{y0}) + \tau\left[2a_x\left(x_k^b - x_0\right)\right. \\ &\left. + 2a_y\left(y_k^b - y_0\right) - v_{x0}^2 - v_{y0}^2\right] \\ &+ \left(x_k^b - x_0\right)v_{x0} + \left(y_k^b - y_0\right)v_{y0} = 0, \end{aligned} \tag{A4}$$

where we have assumed $\tau_0 = 0$ for simplicity. This equation possesses a general solution, provided the ray curvature is small enough. When the ray is almost straight, it is straightforward to show that τ_{jk} reads

$$\tau_{jk} \simeq \frac{v_{x0}\left(x_k^b - x_0\right) + v_{y0}\left(y_k^b - y_0\right)}{v_{x0}^2 + v_{y0}^2}. \tag{A5}$$

The general solution for Eq. (A4) can otherwise be used (it is not written here, for conciseness). The triangle k is considered to be covered by the envelope of the beam if $\tau_{jk} \in [\tau_0,\tau_1]$

(see Fig. 9). A neighborhood search algorithm allows us to perform this computation on triangles neighboring j to improve performances. The distance r_{jk} from the barycenter of triangle k to the central ray in triangle j is then straightforward to compute. The search and energy deposition is considered complete when the triangles found in the intersection are at distances r_{jk} further than $\pm 2w$.

2. Integrations over triangles

The maximum power that can be deposited by the beam while the central ray is in triangle j follows from the integration of the imaginary part of the relative permittivity along the path of the central ray

$$\Delta P^j_{\rm abs} = P^j_1 - P^j_0 = \sqrt{\frac{\pi}{2}}\,(I_1 w_1 - I_0 w_0)$$
$$= \sqrt{\frac{\pi}{2}} I_0 w_0 \left[\exp\left(-2k_0 \int_{\tau_0}^{\tau_1} \epsilon_c''(\tau) d\tau\right) - 1\right], \quad \text{(A6)}$$

where I designates the on-axis intensity. Subscripts 0 and 1 stand for the entrance and exit of the ray in triangle j, respectively. Here $\Delta P^j_{\rm abs}$ is the maximum power that can be deposited from the ray, independently of the mesh configuration. Mesh boundaries can eventually crop the beam, resulting in a total power deposited in the mesh less than $\Delta P^j_{\rm abs}$.

Assuming triangle k has been selected according to the criterion defined in Appendix A 1, the power $P^k_{\rm abs}$ deposited in triangle k is

$$P^k_{\rm abs} = \iint_{A_k} \nu^j_{ei} \frac{\omega_p^2}{\omega_0^2} \frac{\epsilon_0}{2} |u|^2 dA, \quad \text{(A7)}$$

where A_k designates the area of triangle k and we use the value of ν_{ei} from the central ray, i.e., from the triangle j, and $|u|^2 = |u_0(\tau)|^2 e^{-2r^2/w^2(\tau)}$. We note that the sum of all $P^k_{\rm abs}$ over selected triangles always is less than or equal to $\Delta P^j_{\rm abs}$.

In order to integrate Eq. (A7), we make the assumption that u, w, and $\nu_{ei} n_e/n_c$ vary linearly in $[\tau_0, \tau_1]$, between $u_0, w_0, (\nu_{ei} n_e/n_c)_0$ and $u_1, w_1, (\nu_{ei} n_e/n_c)_1$. This approximation remains correct as long as high gradients of laser intensity occur in regions where the mesh is reasonably refined. Once a triangle has been selected, the integration is performed over its entire surface, even if parts of the triangle lie outside of the $[\tau_0, \tau_1]$ range. This is illustrated on Fig. 10 along with the notation used.

Contrary to the triangle selection algorithm detailed in Appendix A 1, we assume for the computation of $P^k_{\rm abs}$ that the ray trajectory between τ_0 and τ_1 is straight. Given a triangle k defined by points (A,B,C), we compute the coordinates (τ_A, τ_B, τ_C) at which the ray normal intersects the triangle points (see Fig. 10). These values are linearly interpolated (or extrapolated) from the given values of τ_0 and τ_1 and the coordinates of the ray. We now rename (A,B,C) so that (τ_A, τ_B, τ_C) is in ascending order. In this framework, $P^k_{\rm abs}$ reads

$$P^k_{\rm abs} = \frac{\epsilon_0 \omega_0}{2} \left(\int_{\tau_A}^{\tau_B} \int_{\mathcal{D}_{AB}(\tau)}^{\mathcal{D}_{AC}(\tau)} \sqrt{\epsilon_j'(\tau)} \epsilon_j'' |u|^2 dq\, d\tau \right.$$
$$\left. + \int_{\tau_B}^{\tau_C} \int_{\mathcal{D}_{BC}(\tau)}^{\mathcal{D}_{AC}(\tau)} \sqrt{\epsilon_j'(\tau)} \epsilon_j'' |u|^2 dq\, d\tau \right), \quad \text{(A8)}$$

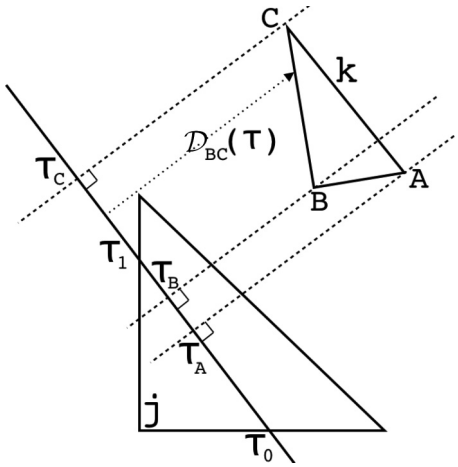

FIG. 10. Illustration of a triangle configuration for the integration of PCGO variables on the hydrodynamical mesh. The central ray is approximated by a straight line and crosses triangle j between τ_0 and τ_1. Dashed lines correspond to normals to the central ray at different values of τ. Distances $\mathcal{D}$ introduced in Eq. (A8) are always taken along the ray normal, as illustrated here with $\mathcal{D}_{\rm BC}(\tau)$.

where we have used $\nu^j_{ei}\omega_p^2/\omega_0^2 = \epsilon_j''\omega_0$ and $\mathcal{D}_{AB}(\tau)$ is the distance between the central ray at τ and the segment AB along the normal of the ray (this notation stands for any segment in triangle ABC). Distances $\mathcal{D}$ are linear expressions of τ by construction:

$$\mathcal{D}_{AB}(\tau) = (\mathcal{D}_B - \mathcal{D}_A)(\tau - \tau_A)/(\tau_B - \tau_A) + \mathcal{D}_A, \quad \text{(A9)}$$

where $\mathcal{D}_A$ is the distance between the central ray at τ_A and the coordinates of the point A, along the ray normal. Equation (A8) can be simplified to

$$P^k_{\rm abs} = \frac{\epsilon_0\omega_0}{4}\sqrt{\frac{\pi}{2}} \left\{ \int_{\tau_A}^{\tau_B} \sqrt{\epsilon_j'(\tau)} \epsilon_j''(\tau) |u_0(\tau)|^2 w(\tau) \right.$$
$$\times \left[\mathrm{erf}\left(\frac{\sqrt{2}\mathcal{D}_{AC}(\tau)}{w(\tau)}\right) - \mathrm{erf}\left(\frac{\sqrt{2}\mathcal{D}_{AB}(\tau)}{w(\tau)}\right)\right] d\tau$$
$$+ \int_{\tau_B}^{\tau_C} \sqrt{\epsilon_j'(\tau)} \epsilon_j''(\tau) |u_0(\tau)|^2 w(\tau)$$
$$\left. \times \left[\mathrm{erf}\left(\frac{\sqrt{2}\mathcal{D}_{AC}(\tau)}{w(\tau)}\right) - \mathrm{erf}\left(\frac{\sqrt{2}\mathcal{D}_{BC}(\tau)}{w(\tau)}\right)\right] d\tau \right\}, \quad \text{(A10)}$$

with

$$\mathcal{F}(\tau) = [\mathcal{F}(\tau_1) - \mathcal{F}(\tau_0)](\tau - \tau_0)/(\tau_1 - \tau_0) + \mathcal{F}(\tau_0), \quad \text{(A11)}$$

where $\mathcal{F}$ is u_0, w, or ϵ_j''. This expression cannot be integrated analytically for linearly varying parameters. Here $P^k_{\rm abs}$ is computed using a numerical integrator based on Romberg's method that is of a higher order than the traditional Simpson rule [27–29].

APPENDIX B: TWO-DIMENSIONAL GAUSSIAN BEAM SELF-FOCUSING EQUATIONS

We present here a brief description of a Gaussian beam undergoing ponderomotive self-focusing in a initially

homogeneous plasma. Such a model was derived for Gaussian beams in cylindrical coordinates in Refs. [19,20]. The formalism developed in Ref. [20] is adapted to a simpler 2D geometry so that the PCGO and RT models can be compared to the theory. Appendix B 1 presents an equation for the evolution of the width of a Gaussian beam undergoing ponderomotive self-focusing in a 2D framework. The corresponding critical power is derived in Appendix B 2.

1. Derivation of the beam width equation

Starting from the wave equation for the electric field as shown in Ref. [19], the electron density on the beam axis is depleted according to

$$n = n_0 \exp\left(-\beta E_0^2\right), \tag{B1}$$

where $\beta = e^2/4m_e w_0^2(T_e + T_i)$ and n_0 is the initial electron density. This formalism holds for length scales L such as $L \gg \lambda_D$ and time scales long compared to L/c_s, where λ_D is the Debye length and c_s is the sound speed. For a plane wave and assuming $n_e/n_c \ll 1$ so that absorption can be neglected, one can derive the following equation for the complex field amplitude u in the paraxial approximation [20]:

$$-2ik_0c^2\frac{\partial u}{\partial z} + c^2\triangle_\perp u - \Gamma^2 u + \omega_{p0}^2 u(1 - \exp -\beta|u|^2) = 0, \tag{B2}$$

where ω_{p0}^2 is the unperturbed plasma frequency, $\Gamma^2 = k_0^2c^2 - \omega_0^2 + \omega_{p0}^2$ represents the nonlinear wave-number shift due to the amplitude depression on the beam axis caused by the ponderomotive force, and z is the propagation axis. Here u is written in term of amplitude u_0 and eikonal S:

$$u = u_0(x,z)\exp[-ik_0S(x,z)], \tag{B3}$$

where x is the transverse direction of the paraxial wave.

Introducing Eq. (B3) in Eq. (B2) and assuming a 2D geometry, we get

$$2\left(\frac{\partial u_0}{\partial z} + \frac{\partial S}{\partial x}\frac{\partial u_0}{\partial x}\right) + u_0\frac{\partial^2 S}{\partial x^2} = 0, \tag{B4}$$

$$c^2\frac{\partial^2 u_0}{\partial x^2} - k_0^2c^2u_0\left[2\frac{\partial S}{\partial z} + \left(\frac{\partial S}{\partial x}\right)^2\right] - \Gamma^2u_0 + \omega_{p0}^2u_0\left[1 - \exp\left(-\beta u_0^2\right)\right] = 0, \tag{B5}$$

which is similar to Eqs. (7) and (8) in Ref. [20], except for the missing cylindrical components of the Laplacian. We now assume a 2D Gaussian profile for u:

$$u_0(x,z) = (E_0/\sqrt{f})\exp\left(-x^2/w_0^2f^2\right), \tag{B6}$$

$$S(x,z) = \frac{x^2}{2}\frac{1}{f}\frac{df}{dz} + \phi, \tag{B7}$$

where $\phi(z)$ is the phase and $f(z)$ is the Gaussian beam shape factor $f(z) = w(z)/w_0$. Note that for a cylindrically symmetric Gaussian beam, $\sqrt{f}$ is replaced by f in the expression of u_0. We can verify that this model is consistent by checking that Eqs. (B6) and (B7) always satisfy (B4). Substitution of this model in Eq. (B5) yields, to zeroth order in r/w_0f,

$$f^2\left[-2c^2k_0^2\phi' - \Gamma^2 - \omega_{p0}^2\exp\left(-\beta E_0^2/f\right) + \omega_{p0}^2\right] - \frac{2c^2}{w_0^2} = 0. \tag{B8}$$

The next order in the expansion is the order 2 in r/w_0f:

$$f\left\{f\left[c^2k_0^2(2\phi' - w_0^2ff'') + \Gamma^2 - \omega_{p0}^2\right] + \omega_{p0}^2\exp\left(-\beta E_0^2/f\right)\left(f - 2\beta E_0^2\right)\right\} + \frac{6c^2}{w_0^2} = 0. \tag{B9}$$

Equation (B8) describes the wave phase, similar to Eq. (12) in Ref. [20], to a factor 1/2 for the first term on the right-hand side:

$$\phi' = -\frac{1}{w_0^2k_0^2f^2} + \frac{\omega_{p0}^2 - \Gamma^2}{2c^2k_0^2} - \frac{\omega_{p0}^2\exp\left(-\beta E_0^2/f\right)}{2c^2k_0^2}. \tag{B10}$$

Injecting the above solution for the phase in Eq. (B9) gives us the shape factor equation

$$f'' = \frac{4}{w_0^4k_0^2f^3} - \frac{2\beta E_0^2\omega_{p0}^2\exp\left(-\beta E_0^2/f\right)}{w_0^2c^2k_0^2f^2}. \tag{B11}$$

Equation (B11) differs from the cylindrically symmetric case by a factor f in the second term on the right-hand side and in the exponential term. These changes reflect the fact that the total power of the beam in a 2D framework varies with $1/f$ and not $1/f^2$. This equation can be solved numerically to find the self-focusing distance z_{sf} of a 2D Gaussian beam propagating in an initially constant density plasma, as well as the intensity amplification ratio $I_0/I_0(\tau = 0) = 1/f(z_{sf})$.

2. Critical power

An expression for the critical power above which a Gaussian beam propagating in an initially constant density media will undergo self-focusing can be derived from Eq. (B11). This threshold corresponds to the power for which the diffraction of the beam is exactly compensated by the refraction due to the density waveguide created by the ponderomotive expelling of electrons from the wave field. Such an equilibrium is obtained for $f = 1$ and $df/dz = d^2f/dz^2 = 0$. It is straightforward to find the expression for the equilibrium radius w_E using Eq. (B11):

$$w_E = \sqrt{2}\frac{c}{\omega_{p0}}\frac{\exp\left(\beta E_0^2/2\right)}{\sqrt{\beta E_0^2}}. \tag{B12}$$

The same expression is obtained in Ref. [20] for a cylindrically symmetric Gaussian beam. The total power carried by a cylindrically symmetric Gaussian beam is $P = (\pi/2)I_0w_0^2$. Using $E_0^2 = 2I_0/(c\epsilon_0\sqrt{1 - n_e/n_c})$ and replacing β by its expression, we get a relation between I_0 and w_0 for $P = P_C$, where P_C is the critical power. Introducing this relation in the

expression for P we get

$$P_C = -cn_c\sqrt{1-n_e/n_c}\pi(T_e+T_i)w_0^2\mathcal{W}\left(\frac{-2c^2}{w_0^2\omega_{p0}^2}\right), \quad \text{(B13)}$$

where $\mathcal{W}(z)$ is the real-valued Lambert W function, i.e., the real solution v such that $v\exp(v) = z$. For a given initial beam thickness w_0, we compute the initial intensity $I_0^{C;w_0}$ of a 2D Gaussian beam, whose power equals the critical power:

$$I_0^{C;w_0} = -cn_c\sqrt{1-n_e/n_c}\sqrt{2\pi}(T_e+T_i)w_0\mathcal{W}\left(\frac{-2c^2}{w_0^2\omega_{p0}^2}\right), \quad \text{(B14)}$$

where $I_0^{C;w_0}$ is expressed in units of W/m.

[1] L. Divol, R. L. Berger, N. B. Meezan, D. H. Froula, S. Dixit, L. J. Suter, and S. H. Glenzer, Phys. Rev. Lett. **100**, 255001 (2008).

[2] D. H. Froula, L. Divol, R. A. London, R. L. Berger, T. Döppner, N. B. Meezan, J. S. Ross, L. J. Suter, C. Sorce, and S. H. Glenzer, Phys. Rev. Lett. **103**, 045006 (2009).

[3] P. Michel, L. Divol, E. A. Williams, S. Weber, C. A. Thomas, D. A. Callahan, S. W. Haan, J. D. Salmonson, S. Dixit, D. E. Hinkel, M. J. Edwards, B. J. MacGowan, J. D. Lindl, S. H. Glenzer, and L. J. Suter, Phys. Rev. Lett. **102**, 025004 (2009).

[4] I. V. Igumenshchev, D. H. Edgell, V. N. Goncharov, J. A. Delettrez, A. V. Maximov, J. F. Myatt, W. Seka, A. Shvydky, S. Skupsky, and C. Stoeckl, Phys. Plasmas **17**, 122708 (2010).

[5] I. V. Igumenshchev *et al.*, Phys. Plasmas **19**, 056314 (2012).

[6] T. B. Kaiser, Phys. Rev. E **61**, 895 (2000).

[7] Y. A. Kravtsov, Radiophys. Quantum Electron. **10**, 719 (1967).

[8] V. M. Babich and V. F. Lazutkin, Top. Math. Phys. **2**, 9 (1968).

[9] G. V. Pereverzev, Rev. Plasma Phys. **19**, 1 (1996).

[10] G. A. Deschamps and P. E. Mast, in *Proc. Symposium on Quasi-Optics* (Polytechnic Press, New York, 1964), pp. 379–395.

[11] H. Kogelnik, Appl. Opt. **4**, 1562 (1965).

[12] L. W. Casperson, Appl. Opt. **12**, 2434 (1973).

[13] Y. A. Kravtsov and P. Berczynski, Stud. Geophys. Geod. **51**, 1 (2007).

[14] Y. A. Kravtsov and N. Y. Zhu, *Theory of Diffraction, Heuristic Approaches*, Alpha Science Series on Wave Phenomena (Alpha Science International, Oxford, 2010).

[15] J. Breil, S. Galera, and P. H. Maire, Comput. Fluids **46**, 161 (2011).

[16] M. M. Popov, Vestn. Leningr. Univ. **22**, 44 (1969) (in Russian).

[17] W. L. Kruer, *The Physics of Laser Plasma Interactions* (Westview, Boulder, 2003).

[18] S. A. Akhmanov, A. P. Sukhorukov, and R. V. Khokhlov, Sov. Phys. Usp. **10**, 609 (1968).

[19] P. Kaw, G. Schmidt, and T. Wilcox, Phys. Fluids **16**, 1522 (1973).

[20] C. E. Max, Phys. Fluids **19**, 74 (1976).

[21] V. V. Eliseev, W. Rozmus, V. T. Tikhonchuk, and C. E. Capjack, Phys. Plasmas **2**, 1712 (1995).

[22] M. Grech, Ph.D. thesis, Université Bordeaux 1, 2007.

[23] J. Garnier, C. Gouédard, and L. Videau, Opt. Commun. **176**, 281 (2000).

[24] O. Morice, Opt. Eng. **42**, 1530 (2003).

[25] O. Morice, X. Ribeyre, and V. Rivoire, in *Third International Conference on Solid State Lasers for Application to Inertial Confinement*, edited by W. Lowdermilk, SPIE Proc. Vol. 3492 (Bellingham, WA, 1999), pp. 832–838.

[26] P. Donnat, CEA report, 1998 (unpublished).

[27] J. Stoer and R. Bulirsch, in *Introduction to Numerical Analysis* (Springer-Verlag, New York, 1980), pp. 3.4–3.5.

[28] G. Dahlquist and A. Bjorck, in *Numerical Methods* (Prentice-Hall, Englewood Cliffs, NJ, 1974), pp. 7.4.1–7.4.2.

[29] A. Ralston and P. Rabinowitz, in *A First Course in Numerical Analysis*, 2nd ed. (McGraw-Hill, New York, 1978), p. 4.10–2.